Automatic sub-precision membrane contact site detection identifies convoluted tubular riboMERCs

Ben Cardoen[1]*, Guang Gao[2]*, Kurt R. Vandevoorde[2]*, Parsa Alan[2], William Liu[2], A. Wayne Vogl[2], Ghassan Hamarneh[1#], Ivan R. Nabi[2,3#]

[1]School of Computing Science, Simon Fraser University, Burnaby, BC, Canada V5A 1S6
[2]Life Sciences Institute, Department of Cellular and Physiological Sciences, University of British Columbia, Vancouver, BC, Canada V6T 1Z3
[3]School of Biomedical Engineering, University of British Columbia, Vancouver, BC, Canada V6T 1Z3

*, # equal contribution
[#] To whom correspondence should be sent: hamarneh@sfu.ca; irnabi@mail.ubc.ca

Running title: riboMERC detection by super-resolution microscopy

Keywords: Membrane contacts, Machine learning, Super-resolution Microscopy, Endoplasmic reticulum, Mitochondria, Gp78

Abstract

The identification and morphological analysis of mitochondria-ER contacts (MERCs) by fluorescent microscopy is limited by sub-pixel resolution inter-organelle distances. Here, application of a novel Membrane Contact Site (MCS) detection algorithm, MCS-DETECT, to 3D STED super-resolution images reconstructs sub-resolution organelle interactions, identifying diverse MERCs. By EM, elongated ribosome-studded riboMERCs are present in HT-1080 but not COS-7 cells and, correspondingly, MCS-DETECT identifies extended large MERCs selectively in HT-1080. These are morphologically distinct from smaller smooth contacts in COS-7 cells and larger contacts induced in COS-7 cells by expression of an mitochondria-ER linker. Large riboMERC expression is reduced in Gp78 knockout HT-1080 cells and their induction by Gp78 in COS-7 cells is dependent on Gp78 ubiquitin ligase activity. Gp78-dependent riboMERCs present complex tubular shapes that intercalate between and contact multiple mitochondria. MCS-DETECT of whole cell super resolution 3D image volumes therefore identifies a novel convoluted tubular morphology for riboMERCs whose formation is dependent on Gp78 ubiquitin ligase activity.

Introduction

In the cell, organelles communicate with each other at membrane contact sites where two membranes come in close proximity, as close as 15-30 nm, without fusing (Helle et al., 2013; Valm et al., 2017). Mitochondria-endoplasmic reticulum contacts (MERCs) are hubs for exchange between the endoplasmic reticulum (ER) and mitochondria, enabling calcium transfer required for mitochondrial enzyme activity and ATP production phospholipid and sterol biosynthesis, mitochondrial dynamics and metabolism as well as the execution of cell death programs (Rowland and Voeltz, 2012). MERCs are closely associated with disease progression, including cancer, neurodegenerative, cardiovascular and other diseases (Barazzuol et al., 2021; Díaz et al., 2021; Markovinovic et al., 2022).

MERCs were traditionally thought to comprise narrow (10-15 nm width) contacts with smooth ER membranes devoid of ribosomes (Goetz and Nabi, 2006; Perkins et al., 1997). Wider (~50 nm) rough ribosome-studded riboMERCs were identified in metastatic HT-1080 fibrosarcoma cells and in HEK293 cells where they are regulated by the Gp78 E3 ubiquitin ligase and interaction between the outer mitochondrial membrane (OMM) protein SYNJ2BP and its ER partner, ribosome-binding protein 1 (RRBP1), respectively (Hung et al., 2017; Wang et al., 2015). RiboMERCs of 25 nm contact distance are found in liver, also called WrappER-associated mitochondria (WAM) as they wrap around mitochondria (Anastasia et al., 2021; Csordas et al., 2006; Giacomello and Pellegrini, 2016; Parlakgül et al., 2020). Other studies have reported MERCs of varying distances ranging from 10-80 nm (Giacomello and Pellegrini, 2016).

The specificity of labeling and ability to study dynamic fluorescent tagged proteins in living cells makes fluorescent microscopy the method of choice to characterize the diversity, dynamics and molecular mechanisms underlying MERC formation. However, analysis of MERCs by fluorescence microscopy faces three major hurdles: 1) the distance between the ER and mitochondria is below the resolution of optical microscopy (200-250 nm) due to diffraction limits; 2) MERC segmentation approaches are sensitive to subjective parameter settings such that accurate thresholding of the ER, ranging from isolated peripheral tubules to the dense central ER matrix, is particularly challenging; 3) bifluorescent complementation systems of varying linker lengths present differential detection of MERCs, but may promote or stabilize MERC formation (Cieri et al., 2018; Harmon et al., 2017; Vallese et al., 2020). Earlier work using diffraction limited confocal microscopy showing that ER tubules mark mitochondrial constrictions (Friedman et al., 2011) has been confirmed using super-resolution single molecule localization microscopy (SMLM) (Shim et al., 2012) and live cell 2D stimulated emission depletion (STED) imaging (Bottanelli et al., 2016). 2D STED characterized roles for ER shaping proteins in control of peripheral ER tubule nanodomains and fenestrations in ER sheets (Gao et al., 2019; Schroeder et al., 2019). 3D super-resolution whole cell analysis by structured illumination (SIM) or 3D STED microscopy achieves ~150 nm lateral and ~250 nm axial resolution and identified tubular matrices in periph-

eral ER sheets and in the dense central ER of Zika virus infected cells (Long et al., 2020; Nixon-Abell et al., 2016). SIM and STED therefore represent optimal super-resolution imaging approaches to study the distribution and morphology of MERCs in 3D whole cell views.

However, the intervening space between ER and mitochondria remains far smaller than the resolution provided by SIM or 3D-STED. In addition, detection of MERCs requires analytical approaches that can accurately assess overlap between two fluorescent channels acquired independently, facing challenges of varying background density and difficulty of thresholding signals of varying signal to noise ratio. Recently, the optimal transport distance between two fluorescence distributions was formulated as an alternative approach to colocalization (Tameling et al., 2021; Wang and Yuan, 2021). However, whether this method is able to recover interactions at sub-precision distances of MERCs is not known. By reducing the anisotropy using multiple unregistered samples and mathematical optimization, more precise colocalization is becoming possible (Fortun et al., 2018); however, this method does not directly quantify sub-precision interfaces. Quantitative detection of MERCs in 3D cell volumes for fluorescent microscopy therefore requires novel analytical approaches that apply sub-pixel resolution detection of interaction zones to whole cell super-resolution imaging approaches. To this end we developed a multichannel differential analysis to reconstruct the interface at sub-pixel precision. Without requiring segmentation, the algorithm adapts robustly to the intensity variations between fluorescent channels and samples, resulting in highly sensitive detection independent of variations in local signal or background intensity differentials. Application to 3D STED super-resolution microscopy images of cells distinguishes different classes of MERCs and defines a role for Gp78 ubiquitin ligase activity in the formation of a distinct class of extended, convoluted, tubular ribosome-associated MERCs (riboMERC).

RESULTS AND DISCUSSION

Distinct MERCs in COS-7 and HT-1080 cells

EM analysis shows the presence of elongated rough ER-mitochondria (RER-mito) contacts in HT-1080 cells, as previously reported (Wang et al., 2015) while COS-7 cells present predominantly shorter, smooth ER-mitochondria (SER-mito) contacts (Fig. 1). Further, SER-mito and RER-mito contacts co-exist in HT-1080 cells as a single unit, with a smaller smooth MERC extending from a more elongated RER-mito contact (Fig. 1A), as previously reported (Giacomello and Pellegrini, 2016; Wang et al., 2015). Defining RER-mito contacts as any contact site containing at least one ribosome within the interorganellar space, we report here a 55 nm spacing between ER and mitochondria of HT-1080 RER-mito contacts and 15 nm spacing of SER-mito contacts, corresponding to our previous study (Wang et al., 2015). In COS-7 cells, RER-mito contacts are ~35 nm in width while SER-mito contacts are ~25 nm in width (Fig. 1B). The different spacing of both classes of MERCs in HT-1080 and COS-7 cells highlights the varied spac-

ing of MERCs in different cells and tissues (Csordas et al., 2006; Giacomello and Pellegrini, 2016; Hung et al., 2017; Parlakgül et al., 2020; Wang et al., 2015).

RER-mito contacts in HT-1080 are of varying length and significantly longer than RER-mito contacts in COS-7 cells or SER-mito contacts in either HT-1080 or COS-7 cells (Fig. 1B). HT-1080 RER-mito contacts extend over almost 30% of the mitochondrial perimeter and contact a significantly larger proportion of mitochondria analyzed compared to SER-mito contacts or COS-7 RER-mito contacts that contact less than 5% of the mitochondrial surface. Almost 70% of HT-1080 MERCs are RER-mito contacts and compose 90% of MERCs in HT-1080 cells by length compared to less than 10% of MERCs in COS-7 cells (Fig. 1C). Importantly, RER-mito contacts of COS-7 cells contained at most 5 ribosomes within the interorganellar space compared to HT-1080 RER-mito contacts, some of which contained up to 25 ribosomes in a single contact (Fig. 1D). Elongated RER-mito contacts containing more than five ribosomes are therefore specific to HT-1080 cells and will heretofore be referred to as riboMERCs (Giacomello and Pellegrini, 2016).

Whole cell 3D STED image stacks of HT-1080 cells transfected with the lumenal ER reporter, ERmoxGFP (Costantini et al., 2015) were fixed with ER-preserving 3% paraformaldehyde/0.2% glutaraldehyde (Gao et al., 2019; Long et al., 2020; Nixon-Abell et al., 2016) and labeled for the outer mitochondrial membrane (OMM) protein TOM20 (Fig. 2A). Overlapping ER-mitochondria signal is observed in the cell periphery and more extensively in the central ER region, that for HT-1080 cells extends across multiple STED sections over 3 microns in depth. COS-7 cells present an abundance of ER-mitochondria overlapping regions but limited central ER overlap with mitochondria (Fig. 2A). The extended ER-mitochondria overlap of HT-1080 cells is consistent with the presence of elongated riboMERCs, as observed by EM (Fig. 1). However, defining actual contact sites from these 3D fluorescent whole cell views is challenging and subjective, based on user-dependent segmentation.

MERC identification by differential channel correlation

Current image segmentation faces challenges of varying background density, difficulty of thresholding signals of varying density and particularly challenging when dealing with the highly varied density and complexity of the ER. In addition, analysis of overlap between two channels is based on separate segmentation of independent channels, compounding the error in capturing interaction. Here, we detect MERCs, below precision of the microscope, by observing how the *relative* intensity of ER and mitochondria labeling change *in tandem*. Images are scanned using a sliding window applying a differential operator to approximate local signal differentials. Interaction between channels colocalizes with the negative Spearman correlation of the image differential (Fig. 2B). Inferring contact zones without requiring segmentation therefore represents a novel approach to detect organelle contacts sites from multi-channel fluorescent images.

An in-silico experiment demonstrates the underlying principle of the method (Fig. 2B). An axial view of the intensity of two spheres acquired with a Gaussian point spread function (PSF) are shown in the upper row and negative Laplacian of the intensity profile of the two objects in the middle row. Distance between the 2 objects is varied from direct interaction up to the system resolution to mimic the MERC reconstruction problem where the interface is below acquisition precision. The detection principle relies on the negative correlation (bottom row, Fig. 2B) of the 2nd intensity differential, approximated by the Laplacian operator. Importantly, the differential Spearman response is present for the entire sub-precision interaction range, confirming that a negative Spearman correlation of the negative Laplacian of the intensity profile corresponds to overlap of two adjacent objects, even when the precision of the system does not allow direct observation.

As shown in Fig. 2C, the correlation principle is one step of a larger sequence of steps that address variable labelling density, low signal to noise ratio, intensity bleeding through multiple Z-slices, and anisotropic precision associated with 3D STED images. A full parameter sensitivity study is performed, with results shown in Supp. Fig. 1A. The full algorithm, including pseudocode and mathematical formulation for each stage, is detailed in Materials and Methods and Supp. Fig. 1B.

Detecting riboMERCs in HT-1080 cells with MCS-DETECT

Application of MCS-DETECT to HT-1080 and COS-7 cells transfected with ERmoxGFP and labeled for mitochondrial TOM20 extracts a mask of contact zones (Fig. 3A). Overlay of the detected contacts on 3D volume rendering of deconvolved STED ER and mitochondria image stacks shows extended perinuclear contact zones in HT-1080 cells and smaller dispersed MERCs along mitochondria in COS-7 cells. Insets show that contact sites are localized to regions of interaction between ER (in green) and mitochondria (in red). 3D STED super-resolution microscopy is anisotropic with a predicted lateral resolution of 120 nm and axial resolution of 250 nm. Each voxel is 25x25x100 nm such that contact zone detection for larger contacts, and particularly for those that are located on top of mitochondria parallel to the plane of the acquired optical section, may be recovered with lower precision. We also detected a large number of contact sites between ER and smaller, reduced intensity TOM20-labeled mitochondrial structures (Supp Fig. 2), that may correspond to mitochondria vesicles (Neuspiel et al., 2008). To ensure that MERC analysis by MCS-DETECT parallels the contact sites detected by EM adjacent to intact mitochondria (Fig. 1), we filtered out these small, low intensity mitochondria labeled structures from the images based on size and intensity (Supp. Fig. 2).

To quantify ER-mitochondria contact zones in HT-1080 and COS-7 cells, we detected, per cell, mitochondria surface coverage ratio and number of mitochondria contacts within a fixed, non-

overlapping, sliding window over the surface of each mitochondrion (Fig. 3B). HT-1080 cells present an approximate two-fold increased coverage of mitochondria and number of contacts per sample region, corresponding closely to the increased mitochondrial surface coverage we observe by EM (Fig. 1B), if one combines the smooth and riboMERC EM data as these are indistinguishable by STED microscopy. Pairwise analysis of MERC features shows that HT-1080 MERCs are on average larger and more spherical than COS-7 MERCs. A clear difference in mean Spearman response and anisotropy supports structural differences between MERCs of HT-1080 and COS-7 cells that show a clear correspondence with our EM results (Fig. 1).

A construct coding for the outer mitochondrial membrane AKAP sequence fused to the ER targeting sequence of Ubc, an OMM-ER linker, induces close contacts (<20 nm) between ER and mitochondria (Csordas et al., 2010; Hajnoczky et al., 2006). Expression of this OMM-ER linker in COS-7 cells induced extended MERCs (Fig. 3A). Mitochondrial surface coverage was increased relative to COS-7 cells but decreased relative to HT-1080 cells. In contrast to the MERCs of HT-1080 cells, a reduction in the number of contact sites per sample region was observed. As for HT-1080 cells, pairwise analysis showed that the MERCs of COS-7 cells expressing the OMM-ER linker were larger and showed distinct groupings compared to COS-7 MERCs with respect to both sphericity and Spearman response. The latter features were not however shifted away from COS-7 to the same extent as HT-1080 MERCs. The OMM-ER linker therefore induces expansion of COS-7 MERCs to form larger MERCs whose features are distinct from the MERCs of riboMERC expressing HT-1080 cells. MCS-DETECT therefore detects MERC features that form a statistically significant signature for diverse type of contacts.

Gp78 regulates riboMERC expression

Using CRISPR/Cas knockout Gp78 HT-1080 cells that present deficient basal mitophagy, impaired mitochondrial health and increased mitochondrial ROS (Alan et al., 2022), we show that loss of Gp78 reduces MERC mitochondrial coverage, approaching the levels observed in COS-7 cells (Fig. 3A). The mitochondria of Gp78 KO cells are more spread than WT HT-1080 cells (Alan et al., 2022) and the dense network of perinuclear MERCs is reduced suggesting that these extended MERCs correspond to riboMERCs. Surface coverage and number of contacts per mitochondrial surface region are significantly reduced relative to HT-1080 cells but remain elevated compared to COS-7 cells (Fig. 3 B). This is consistent with prior EM results showing that Gp78 knockdown does not completely eliminate riboMERCs (Wang et al., 2015) and suggests that other mechanisms regulate riboMERC expression in these cells, such as SYNJ2BP-RRBP1 interaction (Hung et al., 2017). Overexpression of Gp78 in COS-7 cells induces the inverse response in which COS-7 cells gain large contacts similar to those found in HT-1080 cells. Importantly, overexpression of a RING finger mutant of Gp78, Gp78 RM, lacking ubiquitin ligase activity and unable to induce mitophagy (Fang et al., 2001; Fu et al., 2013), is unable to induce this effect. These data indicate that the large contact zones selectively enriched in HT-1080 cells

correspond to riboMERCs and identify Gp78 ubiquitin ligase activity as a specific regulator of these contact sites.

To characterize riboMERCs at the level of individual MERCs, we analyzed the largest 5% of MERCs in each cell, which based on our EM analysis correspond to elongated riboMERCs in HT-1080 cells (Fig. 1). The size of the top 5% of MERCs per cell (Fig. 5A) paralleled our analysis of the average size of all MERCs per cell (Fig. 3B, 4B), a strong indication that differences in contacts across cell lines are driven by changes in the tail (largest) of the contact size distribution. Shape feature analysis of the largest 5% MERCs shows that riboMERCs of HT-1080 cells are taller, more spherical and less planar than the MERCs induced by the OMM-ER linker in COS-7 cells. RiboMERCs of HT-1080 cells form extended, labyrinthine structures that are intercalated between and form contacts with multiple mitochondria (Fig. 5C). The large MERCs induced by the OMM-ER linker form more elongated planar structures that are closely associated with an individual mitochondrion, explaining the decrease in number of contact sites per region observed upon expression of the OMM-ER linker in COS-7 cells (Fig. 3B). Features and structure of large MERCs induced by overexpression of Gp78 in COS-7 cells are similar to that of HT-1080 riboMERCs, demonstrating that Gp78 induces the formation of extended, convoluted, tubular riboMERCs in COS-7 cells (Fig. 5C).

Conclusions

Due to the dense ER structure in the perinuclear region of the cell, fluorescent microscopy analysis of the interaction between ER and mitochondria has focused on peripheral ER tubules (Friedman et al., 2011). Here, using STED super resolution imaging technique and a novel segmentation-free approach to identify membrane contact sites (MCS-DETECT), we identify MERCs in whole cell 3D volumes of HT-1080 and COS-7 cells and further detail the role of Gp78 ubiquitin ligase activity in the abundance and morphology of riboMERCs.

3D EM tomography studies of riboMERCs in liver show that they that wrap completely around mitochondria, covering for 30-100% of associated mitochondria, and were therefore labeled WrappER (Anastasia et al., 2021). In contrast, riboMERCs in HT-1080 cells do not wrap completely around mitochondria. By thin section EM (Fig. 1), riboMERCs form extended contacts along a single face of the mitochondrion that cover at most 30% of the mitochondrion perimeter (Figure 1). While riboMERCs in liver present a sheet-like morphology that wraps around the mitochondrion (Anastasia et al., 2021), 3D STED imaging shows that Gp78-dependent riboMERCs form convoluted, tubular structures resembling tubular matrices (Nixon-Abell et al., 2016) that intercalate between and interact with multiple mitochondria. Consistent with a tubular morphology, the MERCs of HT-1080 and Gp78-transfected COS-7 cells show increased contact sites per analysis window relative to COS-7 cells. In contrast to the tubular Gp78-dependent riboMERCs, MERCs induced by the OMM-ER linker formed more planar structures matching the cap-like

structures induced by these structures by TEM (Csordas et al., 2006). The decrease in contact number for OMM-ER linker expressing COS-7 cells is highly consistent with formation of very tight (<20 nm) extended contacts formed upon expression of this interorganellar linker (Csordas et al., 2006). An increased number of contacts per sliding window could reflect varied distance between ER and mitochondria within the contact, as observed for liver riboMERCs upon knock-down of the riboMERC tether RRBP1 (Anastasia et al., 2021; Hung et al., 2017). While our EM data does detect wider riboMERCs directly connected to narrower SER-mito contacts, the contact width of HT-1080 riboMERCs is very constant ranging from 50-60 nm along the length of the contact (Wang et al., 2015). We interpret this to mean that HT-1080 riboMERCs form extended tubular networks that form multiple contacts with mitochondria.

Indeed, this study highlights the fact that MERCs can take on diverse morphologies. While this analysis focused on a select subset of riboMERCs and a single MERC regulator, Gp78, the large number of MERC tethers identified suggests a high degree of diversity of MERCs, with respect to both function and structure (Giacomello and Pellegrini, 2016; Herrera-Cruz and Simmen, 2017). These studies have been limited by the absence of a robust fluorescence-based approach to detect MERCs. Application of MCS-DETECT to 3D super-resolved volumes of fluorescently labeled cells now provides a means to extend our characterization of MERC diversity, localize MERC tethers to contact sites and study MERC dynamics complementing other criteria used to define membrane contact sites (Scorrano et al., 2019). Importantly, MCS-DETECT is not dependent on expression of MERC reporter molecules and, relative to EM tomography or FIB-SEM, is able to rapidly analyze multiple cell volumes. While we used here 3D STED fixed cell analysis of established models for riboMERC expression to validate the approach, MCS-DETECT reports on negative Laplacians of any two overlapping fluorescent signals and can easily be applied to contacts between any two organelles detected with any voxel-based super-resolution system.

MATERIALS AND METHODS

Cell culture

COS-7 and HT-1080 cells were grown at 37°C with 5% CO_2 in complete RPMI 1640 (Thermo Fisher Scientific, USA) containing 10% FBS (Thermo Fisher Scientific, USA) and 1% L-Glutamine (Thermo Fisher Scientific, USA) unless otherwise stated. Plasmids were transfected using Effectene (Qiagen, Germany) according to the manufacturer's protocols for 22 hours.

Antibodies, plasmids, and chemicals

ERmoxGFP was a gift from Erik Snapp (Addgene plasmid # 68072). Goat serum was purchased from Thermo Fisher Scientific (Cat#: 16210-064), mouse monoclonal (Cat#: ab56783) to TOM20/TOMM20 (1:300 dilution) from Abcam, 16% paraformaldehyde (Cat#: 15710), and 25% glutaraldehyde (Cat#: 16220) were from Electron Microscopy Sciences (Hatfield, PA, USA). Other chemicals were from Sigma.

Electron microscopy

Cells were grown on ACLAR film (Ted Pella) until 80-90% confluency, (1) washed with PBS at room temperature, (2) fixed with 1.5% paraformaldehyde and 1.5% glutaraldehyde in 0.1M sodium cacodylate (Electron Microscopy Sciences, Hatfield, PA, USA), pH 7.3 for 1 h at room temperature followed by 3 washings with 0.1M sodium cacodylate, pH 7.3, (3) postfixed with 1% osmium tetroxide in 0.1M sodium cacodylate buffer for 1 h at 4°C on ice following by 3 washings with H_2O, (4) stained *en bloc* with aqueous 0.1% uranyl acetate for 1 h on ice, (5) progressively dehydrated through an ethanol series (50%, 70%, 90%, and 100%) and 100% propylene oxide (Electron Microscopy Sciences, Hatfield, PA, USA) each for 10 min, (6) infiltrated with 1:1 mixture of EMBED 812 (Electron Microscopy Sciences, Hatfield, PA, USA) and propylene oxide, and embedded in EMBED 812, (7) polymerized for 2 days, (8) sectioned into 50–60 nm thick slices using Leica Ultramicrotome (Leica Microsystems, Wetzlar, Germany), (9) stained with uranyl acetate and lead citrate, (10) imaged on a FEI Tecnai G2 transmission electron microscope (acceleration voltage: 120 kV) and recorded with an Eagle 4k CCD camera (FEI).

Immunofluorescence labeling

Cells grown on #1.5H coverslips (Paul Marienfeld, Germany) were: 1) fixed with 3% paraformaldehyde with 0.2% glutaraldehyde at room temperature for 15 minutes and washed with PBS-CM (phosphate buffer solution supplemented with 1mM $CaCl_2$ and 10mM $MgCl_2$) (two quick washes and then two 5 minute washes); 2) permeabilized with 0.2% Triton X-100 for 5 minutes

then washed with PBS-CM as above; 3) quenched with 1mg/mL of $NaBH_4$ for 10 minutes and washed with PBS-CM; 4) blocked with 10% Goat Serum (Thermo Fisher Scientific, USA) and 1% bovine serum albumin (Sigma, USA) in PBS-CM for 1 hour; 5) incubated with primary antibodies in Antibody Buffer (1% BSA, 2% goat serum, 0.05% Triton-X100, 20X sodium/sodium citrate buffer in Milli-Q H_2O) overnight at 4°C then washed quickly with PBS-CM then three times for 5 minutes with Antibody wash buffer (20x SSC, 0.05% Triton-X100 in Milli-Q H_2O); 6) incubated with secondary antibodies in Antibody Buffer for 1 h then washed quickly with PBS-CM then six times for 10 minutes with Antibody Wash Buffer on a rocker; 7) rinsed with Milli-Q H_2O and mounted with ProLong Diamond (Thermo Fisher Scientific, USA) and cured for 24-48 hours at room temperature.

gSTED microscopy

gSTED imaging were performed with the 100X/1.4 Oil HC PL APO CS2 objective of a Leica TCS SP8 3X STED microscope (Leica, Germany) using white light laser excitation, HyD detectors, and Leica Application Suite X (LAS X) software. Time-gated fluorescence detection was used for STED to further improve lateral resolution. For double labeled fixed samples, the acquisition was done at a scan speed of 600Hz with a line average of 3. GFP was excited at 488 nm and depleted using the 592 nm depletion laser. Alex Fluor 568 was excited at 577 nm and depleted using the 660nm depletion laser. Sequential acquisition (in the orders of AF568/GFP) between frames/stacks was used to avoid crosstalk. STED images were deconvolved using Huygens Professional software (Scientific Volume Imaging, Netherlands).

MCS-DETECT: Contact zone detection pipeline

Illustrated in Figure 2C, the algorithm is composed of 3 steps: computing correlation of intensity and Laplacian for both channels, computing the confidence map, and finally filtering to remove artifacts. A full listing in pseudocode of each stage is provided in Supp. Fig. 1B.

Spearman correlation

We retain the negative Spearman response on the negative Laplacian of each channel (Supp. Fig 1B Alg. 1, 3). In order to prevent the inclusion of low intensity signals colocalizing with high intensity signals, we compute the negative Spearman response of the intensity of both channels; only where both Laplacian and intensity correlate, do we retain the Laplacian correlation.

Confidence map

For each Spearman response voxel, we compute its significance and the minimum observable correlation (Supp. Fig. 1B; Alg. 4, 5), given the sample size (window), using a z-test. Typical

values used here are 0.05 both for alpha and statistical power (1-beta). In Supp. Fig. 1A we show that this parameter leads to consistent results on representative cells.

Filtering

Because 3D STED microscopy is often anisotropic in its point spread function, and one thus risks 'bleed through' across z-planes, we apply a 'bleedthrough' filter (Supp. Fig. 1B; Alg. 2) as a mask by filtering out intensity lower than a given z-score (standard score of intensity), where z is the parameter set in the filter. Bleed-through intensity values will have markedly smaller z-values compared to ER and mitochondria segments. Because the z-score is a pivotal quantity, it will adapt to each channel's distribution and thus lead to an unbiased filter. We test the effect of this filter in Supp. Fig. 1B, where consistent results are retained across a large range of the parameter. Due to low SNR and pixelation, a 'shadowing' response, parallel at an offset of 3-4 voxels to a true response, can appear. As can be observed from the Laplacian curves in Fig 2-B (middle row), voxels where only Laplacian of only one channel changes cannot colocate with a contact. Our gradient filter computes the change of the Laplacian by way of the 3rd derivative of intensity. Next, we mask out any voxels where this 3rd derivative is 0 for 1 channel, yet nonzero for the other. The interested reader can infer from Fig. 2B that a 3rd derivative can be zero for a valid contact, but only if both are zero.

To ensure that we report on contacts with whole mitochondria and not mitochondria fragments or vesicles, as we do by EM, we exclude contacts that are adjacent to mitochondria below a size and mean intensity threshold of respectively 9 (ln scale, voxels) and 0.2, chosen based on empirical observation of non-target mitochondria-labeled segments. We illustrate that these thresholds split the distribution of mitochondria between mitochondria and vesicle-like objects in Supp. Fig. 2. For both COS-7 and HT1080 cells a clear bimodal distribution of mitochondria segments is separable.

Quantifying Contacts

We compute features of contacts sampled by both a sliding window and per-contact. Contacts are distributed with a frequency strongly inverse to their size. Quantifying such long tail distributions can undercount the visually more apparent large contacts. To this end we slide a non-overlapping window over the contact channel and record size and frequency per cube, estimating local density. At the whole contact level we record the confidence, shape, size, and spatial distribution of the contacts. The resulting 2 sets of features allow the end user a local and global descriptive view of contacts in the cell.

For our data we use a sliding window of 25x25x5 voxels, which equates to a cube given the anisotropy of the acquisition. We show in the Supp. Fig. 2A how this window size does not alter the

consistency of our results. We average results over cells and test the result with a non-parametric two-sided Mann Whitney test. Applying multiple testing correction is not practical here, given that we have a pairwise (HT-1080), and 3 pairwise comparisons (COS-7), meaning the correction would be applied only to COS-7 we would be reporting results of COS-7 with a risk of false negative higher than for HT-1080. Contacts are analyzed both by sampling the image, but also as a whole. Large contacts are defined as those exceeding the 95th quantile of volume, per cell. Contacts with size <= 2 voxels are removed, as they are below the diffraction limit. We compute shape features (sphericity, anisotropy, planarity) based on the eigenvalues of the Spearman weighted contacts. Not reported but provided to users of MCS-DETECT are: confidence of reconstruction, clustering, position in Z, to name a few.

Statistical Analysis

Statistical tests are always computed on aggregated (per cell) results to avoid breaking the independence assumption or inducing Simpson's paradox. No outlier removal is performed. Plots are edited for cosmetic alterations only. To avoid dependence on the (partial) presence of the normal distribution, we use the non-parametric 2-sided Mann Whitney test for comparison.

Runtime and memory constraints and its consequences for parameters

The detection algorithm uses a window of size w, for 3D leading to a total window size of $(2*w+1)^3$ voxels. For our results we set w to 2, so each window is 125 voxels large. Let N = X x Y x Z, the dimensions of both channels, and $M = (2*w+1)^3$. Time complexity is dominated by the Spearman correlation, which needs to be applied N times, leading to O(N M log M) complexity. Space complexity is linear in N, however, to offer the end user maximal interpretability we output multiple intermediate stages, leading to an estimated memory use of ~ 10 * N. For our data, depending on the cell size, memory usage averages between 32 and 128GB. The complexity analysis is essential to illustrate why we set w=2. A window size determines directly the minimum observable Spearman response. Larger windows therefore can detect fainter responses. However, a large window risks including multiple interaction patterns, for example, when an interaction zone is enclosed by 2 mitochondria. In such cases the response of both would cancel out the desired response, and we would lose information. The complexity analysis shows that increasing w leads to a cubic increase in runtime. All of these reasons lead us to use a window of 2, spanning ~ 350 nm.

Limitations

It is important to frame the proposed contribution within its limitations. First, any misaligned or unregistered channels can induce false responses or, more likely, cause contact detection to fail. Normalization of both input channels can destroy reconstruction and is not needed, as each stage

is already adapting to the relative intensity distribution. Similarly, if the deconvolution is not calibrated correctly to match the empirical PSF, reconstruction can be compromised. Second, the recovery of sub-precision information is only possible because we exploit the local differential intensity profile of each voxel over a given window. If the signal to noise ratio is too low, differential analysis can break down. If the precision of the system decreases, or spans many voxels, the localization of the interface will become more challenging. For example, from Figure 2B it can be deduced that if the two intensity profiles widen too much, the negative correlation vanishes when their negative 2nd differentials no longer overlap. This phenomenon will become more likely when object size decreases with respect to the width of the interface. For instance, while MCS-DETECT can in principle be applied to diffraction limited samples, recall of interfaces would be less precise. As shown in Figures 3, 4 and 5, two-fold improved resolution of 3D STED image stacks effectively enabled detection of MERCs, that present a 3-10 fold reduced width compared to the resolution of the system. Similarly, a too large window size can destroy a response, for instance when the window spans the size of both objects. In this case positive and negative differentials cancel each other out. Finally, anisotropic precision leads to responses that are less precise in the axis where precision is lowest. In our case precision is worst in Z, so recovered contact sites on top of mitochondria are likely to be captured with reduced precision. Finally, note that MCS-DETECT does not separate proximate contacts that a user could segment as two or more individual adjacent contacts. In future work a more refined approach will tackle the per-region identification even for proximate contacts, but this is limited by ground truth voxels annotated for specific contacts.

FIGURE LEGENDS

Figure 1 Quantitative EM analysis of ER-mitochondria contacts in HT-1080 and COS-7 cells. A) Representative EM images of HT-1080 and COS-7 cells. Insets show RER-mitochondria contacts (RER-mito) in HT-1080 cells and SER-mitochondria contacts (SER-Mito) in COS-7 cells. B) Quantification of contact width, contact length, contact length relative to mitochondria perimeter and number of contacts per mitochondria profile are shown for SER-mito and RER-mito contacts in HT1080 and COS-7 cells. C) The relative ratio of SER-mito and RER-mito contacts in HT-1080 and COS-7 cells based on number of contacts per mitochondria or length of contacts. D) The number of ribosomes vs length per RER-mito contact is plotted for HT-1080 and COS-7 cells. RER-mito contacts with five or less ribosomes are shown in red; those with more than five ribosomes are specific to HT-1080 cells are shown in blue and defined as riboMERCs (+/-SEM; *** $p < 0.001$; **** $p < 0.0001$; Bar = 500 nm).

Figure 2 MCS-DETECT analysis of sub-precision contacts. A) 3D STED images of HT-1080 and COS-7 showing overlap between mitochondria (red) and ER (green). Insets show STED sections at 0.5 uM Z spacing. B) Two objects (red, green discs) are shown at corresponding sub-precision distances. Intensity profiles (top-row), 2nd derivatives (Laplacian), and Spearman correlations of the negative part of the Laplacian (bottom row) are shown. Note how the Spearman response overlaps and changes consistently with the sub-precision distance. C) The detection algorithm (orange) with additional stages that each address a specific confounding factor introduced by the acquisition (bleedthrough) or sample (vesicle removal).

Figure 3 Sub-precision contact detection identifies distinct contact profiles in HT-1080 and COS-7 cells. A) Volume rendered MCS-DETECT views of cells expressing ERmoxGFP (green) and labelled for TOM20 (red) with contact sites overlaid (white) are shown for COS-7, HT-1080 and OMM-ER linker transfected COS-7 cells ROIs from the whole view image are shown volume rendered in adjacent panels. COS-7 mitochondria display numerous small contact zones while mitochondria in HT-1080 and OMM-ER linker transfected COS-7 cells present more extended contact zones. B) Mitochondria surface coverage ratio and the number of contacts per sampled mitochondria window are shown for contact zones in COS-7, HT-1080 and OMM-ER linker transfected COS-7 cells. C) 2D KDE plots of mean contact size over mean anisotropy and mean spearman response, with a linear regression overlayed, are shown for COS-7 (red) vs HT-1080 (blue) cells or COS-7 (red) vs OMM-ER linker transfected COS-7 (blue) cells. (Averaged over cell, two-sided non-parametric Mann Whitney test, n=3; * $p < 005$; *** $p < 0.001$; Bar = 10 µm whole cell; 1 µm insets).

Figure 4 Gp78 regulation of riboMERCs. A) Volume rendered MCS-DETECT views of cells expressing ERmoxGFP (green) and labelled for TOM20 (red) with contact sites overlaid (white) are shown for HT-1080 and Gp78 KO HT-1080 cells and for untransfected COS-7 cells and

COS-7 cells overexpressing wild-type (WT) Gp78 or RING-finger domain mutated Gp78 (Gp78 RM). B) Mitochondria surface coverage ratio and the number of contacts per sampled mitochondria window are shown for contact zones in HT-1080 and Gp78 KO HT-1080 cells and for untransfected COS-7 cells and COS-7 cells overexpressing Gp78 WT or Gp78 RM. C) 2D KDE plots of mean contact size over mean anisotropy and mean spearman response, with a linear regression overlayed, are shown for HT-1080 (blue) vs Gp78 KO HT-1080 (green) cells or COS-7 (red) vs COS-7 overexpressing either Gp78 WT (green) or Gp78 RM (blue). (Averaged over cell, two-sided non-parametric Mann Whitney test, n=3; * $p < 0.05$; ** $p < 0.01$; *** $p < 0.001$; Bar = 10 µm whole cell; 1 µm insets).

Figure 5 Gp78 induces convoluted, tubular riboMERCs A) The 95th quantile (Q95V) of MERC volume per cell is shown for HT-1080 (blue) and Gp78 KO HT-1080 (green) cells, COS-7 (red) and COS-7 overexpressing either Gp78 WT (green) or Gp78 RM (blue), and COS-7 (red) and COS-7 overexpressing the OMM-ER linker (black), representing an unambiguous indicator showing that the largest 5% of contacts are those that differentiate the cell lines studied. B) A representative cell whose Q95V is closest to the mean Q95V of the HT-1080 (blue) cells and COS-7 cells overexpressing either the OMM-ER linker (black) or Gp78 WT (green) was selected for analysis. For the Q95V contacts of each cell we compute shape features: height, sphericity and planarity. The comparison shows that the COS-7 OMM-ER linker induced contacts have a markedly different shape signature compared to those present in HT-1080 and COS-7 Gp78OE (i.e. riboMERCS). C) Representative views of Q95V MERCs (white) from HT-1080 cells and COS-7 cells expressing wither the OMM-ER linker or wild-type Gp78 are shown alone or adjacent to transparent (pink) or solid mitochondria (red) to highlight intercalation of riboMERCs with mitochondria. Rotating videos of these MERCs are attached as Supplemental Videos. Bar = 1 µM.

Alan, P., K. Vandevoorde, B. Joshi, B. Cardoen, Y. Mohammadzadeh, G. Gao, G. Hamarneh, and I.R. Nabi. 2022. Basal Gp78-dependent mitophagy promotes mitochondrial health and limits mitochondrial ROS. *Submitted*.

Anastasia, I., N. Ilacqua, A. Raimondi, P. Lemieux, R. Ghandehari-Alavijeh, G. Faure, S.L. Mekhedov, K.J. Williams, F. Caicci, G. Valle, M. Giacomello, A.D. Quiroga, R. Lehner, M.J. Miksis, K. Toth, T.Q. de Aguiar Vallim, E.V. Koonin, L. Scorrano, and L. Pellegrini. 2021. Mitochondria-rough-ER contacts in the liver regulate systemic lipid homeostasis. *Cell Rep*. 34:108873.

Barazzuol, L., F. Giamogante, and T. Calì. 2021. Mitochondria Associated Membranes (MAMs): Architecture and physiopathological role. *Cell Calcium*. 94:102343.

Bottanelli, F., E.B. Kromann, E.S. Allgeyer, R.S. Erdmann, S. Wood Baguley, G. Sirinakis, A. Schepartz, D. Baddeley, D.K. Toomre, J.E. Rothman, and J. Bewersdorf. 2016. Two-colour live-cell nanoscale imaging of intracellular targets. *Nat Commun*. 7:10778.

Cieri, D., M. Vicario, M. Giacomello, F. Vallese, R. Filadi, T. Wagner, T. Pozzan, P. Pizzo, L. Scorrano, M. Brini, and T. Cali. 2018. SPLICS: a split green fluorescent protein-based contact site sensor for narrow and wide heterotypic organelle juxtaposition. *Cell Death Differ*. 25:1131-1145.

Costantini, L.M., M. Baloban, M.L. Markwardt, M. Rizzo, F. Guo, V.V. Verkhusha, and E.L. Snapp. 2015. A palette of fluorescent proteins optimized for diverse cellular environments. *Nature Communications*. 6:7670.

Csordas, G., C. Renken, P. Varnai, L. Walter, D. Weaver, K.F. Buttle, T. Balla, C.A. Mannella, and G. Hajnoczky. 2006. Structural and functional features and significance of the physical linkage between ER and mitochondria. *J Cell Biol*. 174:915-921.

Csordas, G., P. Varnai, T. Golenar, S. Roy, G. Purkins, T.G. Schneider, T. Balla, and G. Hajnoczky. 2010. Imaging interorganelle contacts and local calcium dynamics at the ER-mitochondrial interface. *Mol Cell*. 39:121-132.

Díaz, P., A. Sandoval-Bórquez, R. Bravo-Sagua, A.F.G. Quest, and S. Lavandero. 2021. Perspectives on Organelle Interaction, Protein Dysregulation, and Cancer Disease. *Front Cell Dev Biol*. 9:613336.

Fang, S., M. Ferrone, C. Yang, J.P. Jensen, S. Tiwari, and A.M. Weissman. 2001. The tumor autocrine motility factor receptor, gp78, is a ubiquitin protein ligase implicated in degradation from the endoplasmic reticulum. *Proc Natl Acad Sci U S A*. 98:14422-14427.

Fortun, D., P. Guichard, V. Hamel, C.O.S. Sorzano, N. Banterle, P. Gönczy, and M. Unser. 2018. Reconstruction from multiple particles for 3D isotropic resolution in fluorescence microscopy. *IEEE transactions on medical imaging*. 37:1235-1246.

Friedman, J.R., L.L. Lackner, M. West, J.R. Dibenedetto, J. Nunnari, and G.K. Voeltz. 2011. ER Tubules Mark Sites of Mitochondrial Division. *Science*. 334:358-362.

Fu, M., P. St-Pierre, J. Shankar, P.T. Wang, B. Joshi, and I.R. Nabi. 2013. Regulation of mitophagy by the Gp78 E3 ubiquitin ligase. *Mol Biol Cell*. 24:1153-1162.

Gao, G., C. Zhu, E. Liu, and I.R. Nabi. 2019. Reticulon and CLIMP-63 control nanodomain organization of peripheral ER tubules. *PLOS Biology*. 17:e3000355.

Giacomello, M., and L. Pellegrini. 2016. The coming of age of the mitochondria-ER contact: a matter of thickness. *Cell Death Differ*. 23:1417-1427.

Goetz, J.G., and I.R. Nabi. 2006. Interaction of the smooth endoplasmic reticulum and mitochondria. *Biochem Soc Trans*. 340:370-373.

Hajnoczky, G., G. Csordas, S. Das, C. Garcia-Perez, M. Saotome, S. Sinha Roy, and M. Yi. 2006. Mitochondrial calcium signalling and cell death: approaches for assessing the role of mitochondrial Ca2+ uptake in apoptosis. *Cell Calcium*. 40:553-560.

Harmon, M., P. Larkman, G. Hardingham, M. Jackson, and P. Skehel. 2017. A Bi-fluorescence complementation system to detect associations between the Endoplasmic reticulum and mitochondria. *Scientific Reports*. 7:17467.

Helle, S.C., G. Kanfer, K. Kolar, A. Lang, A.H. Michel, and B. Kornmann. 2013. Organization and function of membrane contact sites. *Biochim Biophys Acta*. 1833:2526-2541.

Herrera-Cruz, M.S., and T. Simmen. 2017. Of yeast, mice and men: MAMs come in two flavors. *Biol Direct*. 12:3.

Hung, V., S.S. Lam, N.D. Udeshi, T. Svinkina, G. Guzman, V.K. Mootha, S.A. Carr, and A.Y. Ting. 2017. Proteomic mapping of cytosol-facing outer mitochondrial and ER membranes in living human cells by proximity biotinylation. *Elife*. 6:e24463.

Long, R.K.M., K.P. Moriarty, B. Cardoen, G. Gao, A.W. Vogl, F. Jean, G. Hamarneh, and I.R. Nabi. 2020. Super resolution microscopy and deep learning identify Zika virus reorganization of the endoplasmic reticulum. *Scientific Reports*. 10:20937.

Markovinovic, A., J. Greig, S.M. Martín-Guerrero, S. Salam, and S. Paillusson. 2022. Endoplasmic reticulum-mitochondria signaling in neurons and neurodegenerative diseases. *J Cell Sci*. 135.

Neuspiel, M., A.C. Schauss, E. Braschi, R. Zunino, P. Rippstein, R.A. Rachubinski, M.A. Andrade-Navarro, and H.M. McBride. 2008. Cargo-selected transport from the mitochondria to peroxisomes is mediated by vesicular carriers. *Curr Biol*. 18:102-108.

Nixon-Abell, J., C.J. Obara, A.V. Weigel, D. Li, W.R. Legant, C.S. Xu, H.A. Pasolli, K. Harvey, H.F. Hess, E. Betzig, C. Blackstone, and J. Lippincott-Schwartz. 2016. Increased spatiotemporal resolution reveals highly dynamic dense tubular matrices in the peripheral ER. *Science*. 354:3928.

Parlakgül, G., A.P. Arruda, E. Cagampan, S. Pang, E. Güney, Y. Lee, H.F. Hess, C.S. Xu, and G.S. Hotamışlıgil. 2020. High resolution 3D imaging of liver reveals a central role for subcellular architectural organization in metabolism. *bioRxiv*:2020.2011.2018.387803.

Perkins, G., C. Renken, M.E. Martone, S.J. Young, M. Ellisman, and T. Frey. 1997. Electron tomography of neuronal mitochondria: three-dimensional structure and organization of cristae and membrane contacts. *Journal of Structural Biology*. 119:260-272.

Rowland, A.A., and G.K. Voeltz. 2012. Endoplasmic reticulum-mitochondria contacts: function of the junction. *Nat Rev Mol Cell Biol*. 13:607-625.

Schroeder, L.K., A.E.S. Barentine, H. Merta, S. Schweighofer, Y. Zhang, D. Baddeley, J. Bewersdorf, and S. Bahmanyar. 2019. Dynamic nanoscale morphology of the ER surveyed by STED microscopy. *J Cell Biol*. 218:83-96.

Scorrano, L., M.A. De Matteis, S. Emr, F. Giordano, G. Hajnóczky, B. Kornmann, L.L. Lackner, T.P. Levine, L. Pellegrini, K. Reinisch, R. Rizzuto, T. Simmen, H. Stenmark, C. Ungermann, and M. Schuldiner. 2019. Coming together to define membrane contact sites. *Nature Communications*. 10:1287.

Shim, S.H., C. Xia, G. Zhong, H.P. Babcock, J.C. Vaughan, B. Huang, X. Wang, C. Xu, G.Q. Bi, and X. Zhuang. 2012. Super-resolution fluorescence imaging of organelles in live cells with photoswitchable membrane probes. *Proc Natl Acad Sci U S A*. 109:13978-13983.

Tameling, C., S. Stoldt, T. Stephan, J. Naas, S. Jakobs, and A. Munk. 2021. Colocalization for super-resolution microscopy via optimal transport. *Nature Computational Science*. 1:199-211.

Vallese, F., C. Catoni, D. Cieri, L. Barazzuol, O. Ramirez, V. Calore, M. Bonora, F. Giamogante, P. Pinton, M. Brini, and T. Cali. 2020. An expanded palette of improved SPLICS reporters detects multiple organelle contacts in vitro and in vivo. *Nat Commun*. 11:6069.

Valm, A.M., S. Cohen, W.R. Legant, J. Melunis, U. Hershberg, E. Wait, A.R. Cohen, M.W. Davidson, E. Betzig, and J. Lippincott-Schwartz. 2017. Applying systems-level spectral imaging and analysis to reveal the organelle interactome. *Nature*. 546:162-167.

Wang, P.T., P.O. Garcin, M. Fu, M. Masoudi, P. St-Pierre, N. Pante, and I.R. Nabi. 2015. Distinct mechanisms controlling rough and smooth endoplasmic reticulum contacts with mitochondria. *J Cell Sci*. 128:2759-2765.

Wang, S., and M. Yuan. 2021. Revisiting colocalization via optimal transport. *Nature Computational Science*. 1:177-178.

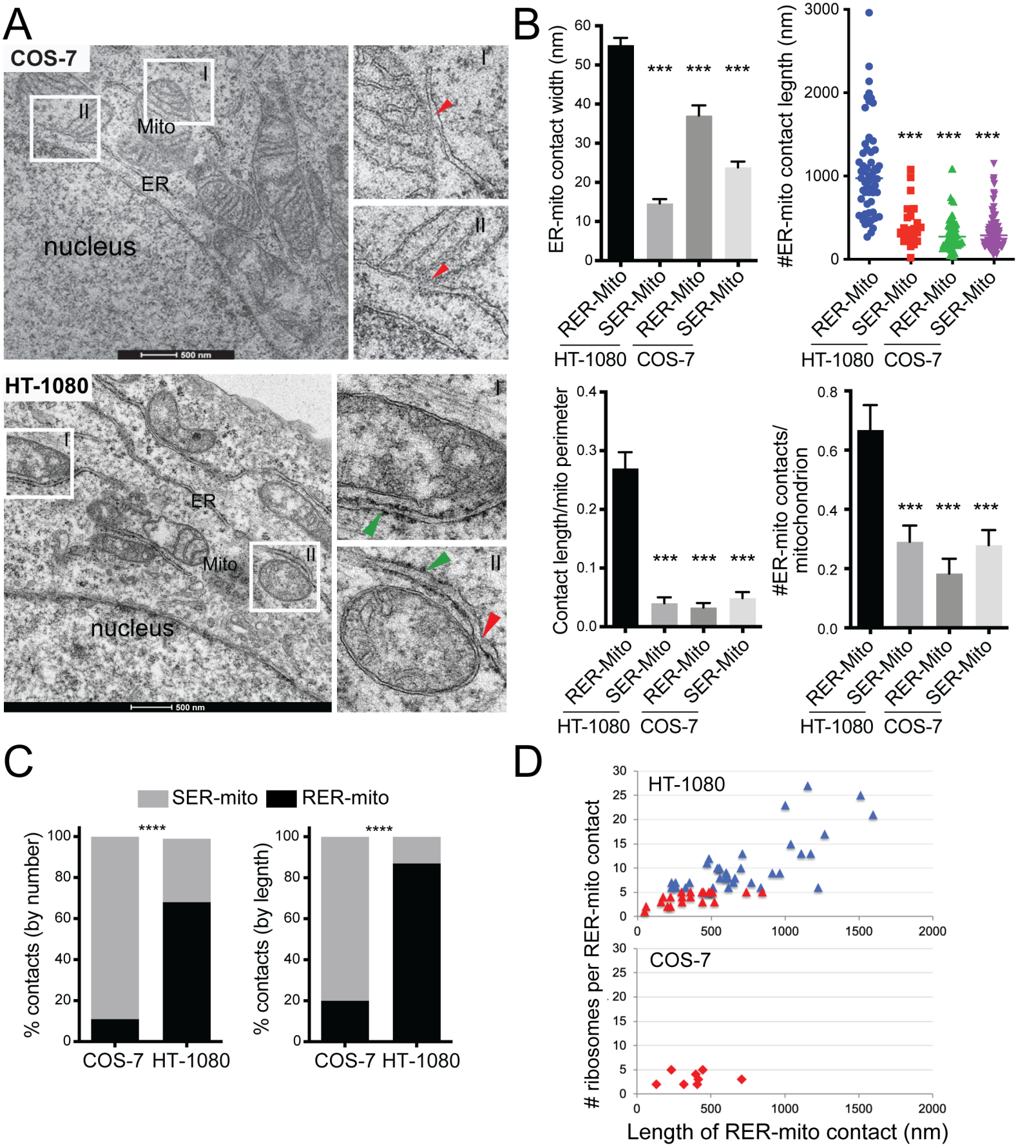
A
COS-7
I
II
Mito
ER
nucleus
500 nm
HT-1080
B
ER-mito contact width (nm)
#ER-mito contact legnth (nm)
Contact length/mito perimeter
#ER-mito contacts/ mitochondrion
RER-Mito
SER-Mito
HT-1080
COS-7
***
C
SER-mito
RER-mito
% contacts (by number)
% contacts (by legnth)
****
D
HT-1080
COS-7
ribosomes per RER-mito contact
Length of RER-mito contact (nm)

Figure 1

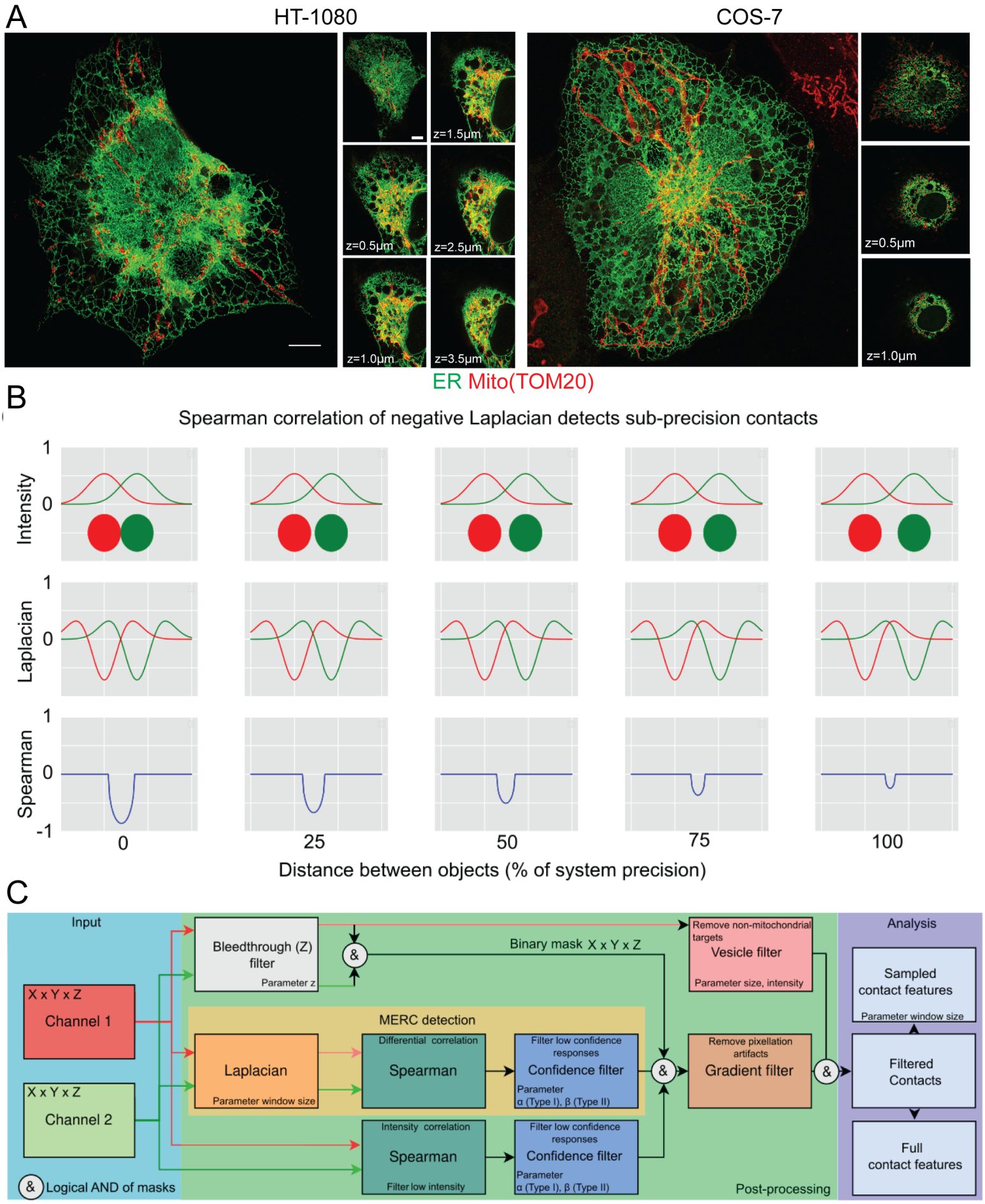
A
HT-1080
COS-7
z=1.5µm
z=0.5µm
z=2.5µm
z=1.0µm
z=3.5µm
z=0.5µm
z=1.0µm
ER Mito(TOM20)
B
Spearman correlation of negative Laplacian detects sub-precision contacts
Intensity
Laplacian
Spearman
1
0
-1
0
25
50
75
100
Distance between objects (% of system precision)
C
Input
X x Y x Z
Channel 1
X x Y x Z
Channel 2
Logical AND of masks
Bleedthrough (Z) filter
Parameter z
Binary mask X x Y x Z
MERC detection
Laplacian
Parameter window size
Differential correlation
Spearman
Filter low confidence responses
Confidence filter
Parameter
α (Type I), β (Type II)
Intensity correlation
Spearman
Filter low intensity
Filter low confidence responses
Confidence filter
Parameter
α (Type I), β (Type II)
Remove non-mitochondrial targets
Vesicle filter
Parameter size, intensity
Remove pixellation artifacts
Gradient filter
Post-processing
Analysis
Sampled contact features
Parameter window size
Filtered Contacts
Full contact features

Figure 2

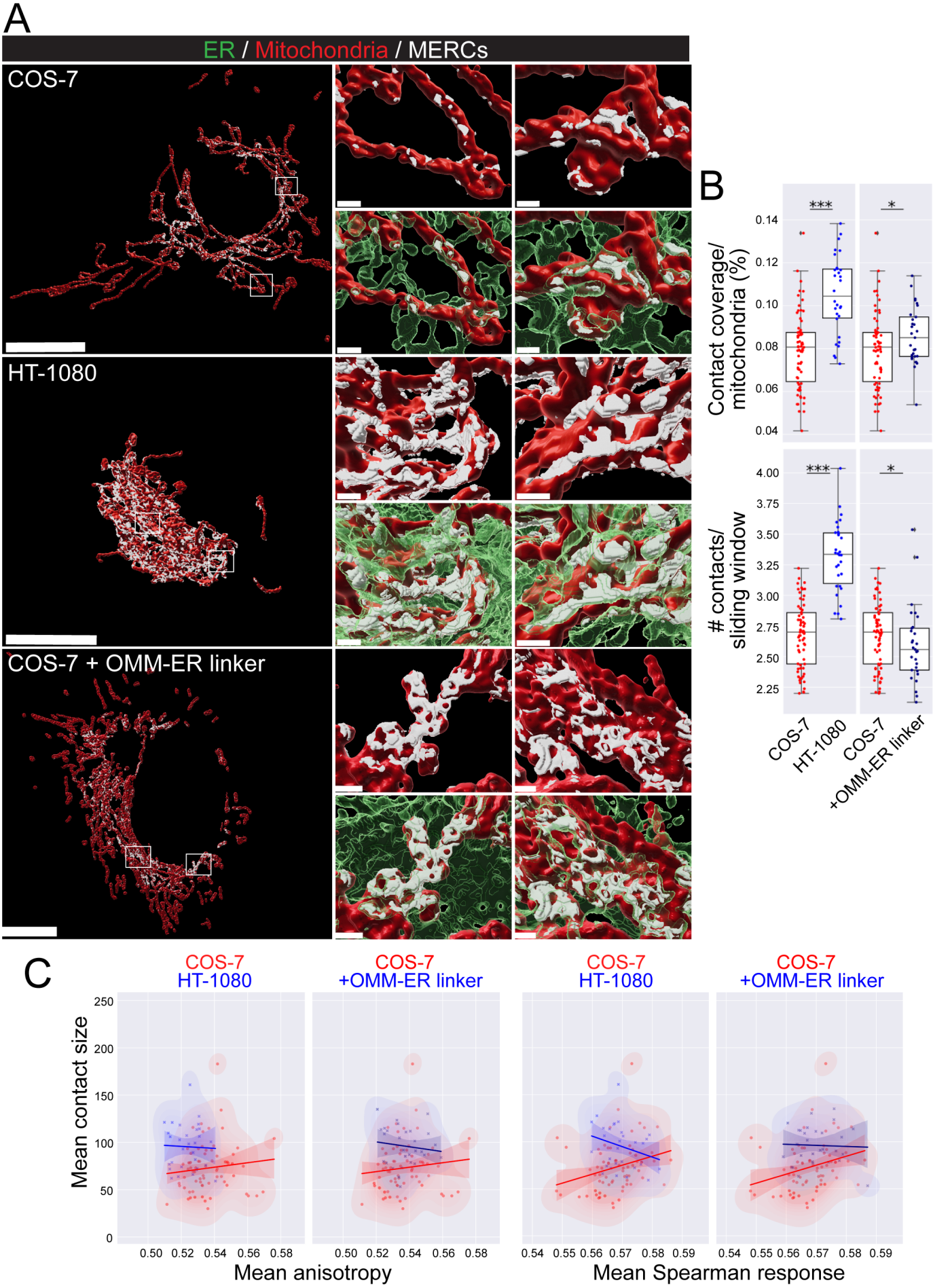
A
ER / Mitochondria / MERCs
COS-7
HT-1080
COS-7 + OMM-ER linker
B
Contact coverage/ mitochondria (%)
contacts/ sliding window
***
*
COS-7
HT-1080
COS-7
+OMM-ER linker
C
COS-7
HT-1080
COS-7
+OMM-ER linker
Mean contact size
Mean anisotropy
Mean Spearman response

Figure 3

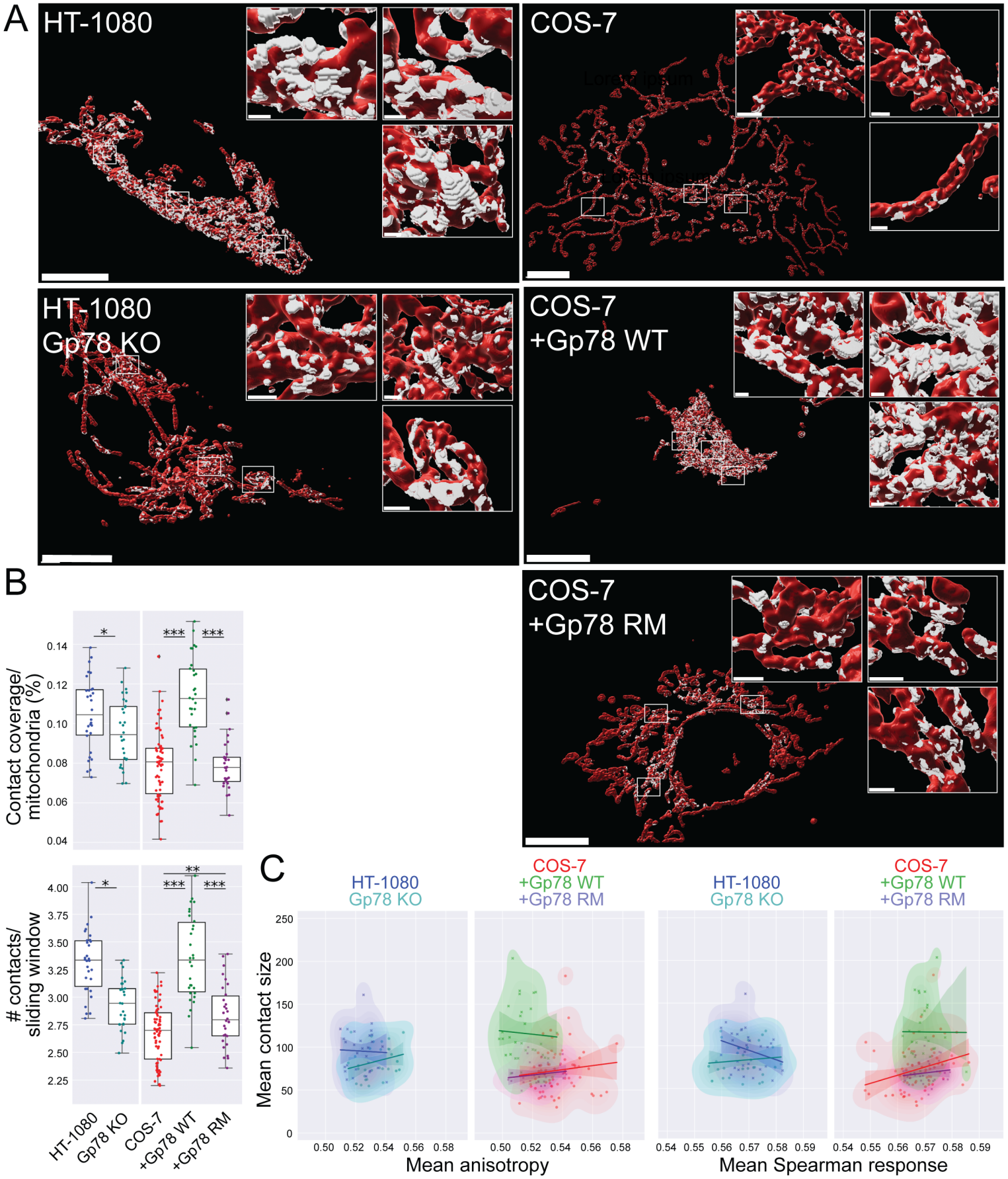
A
HT-1080
COS-7
HT-1080
Gp78 KO
COS-7
+Gp78 WT
COS-7
+Gp78 RM
B
Contact coverage/
mitochondria (%)
0.14
0.12
0.10
0.08
0.06
0.04
*
***
***
contacts/
sliding window
4.00
3.75
3.50
3.25
3.00
2.75
2.50
2.25
*
**
***
***
HT-1080
Gp78 KO
COS-7
+Gp78 WT
+Gp78 RM
C
HT-1080
Gp78 KO
COS-7
+Gp78 WT
+Gp78 RM
HT-1080
Gp78 KO
COS-7
+Gp78 WT
+Gp78 RM
Mean contact size
250
200
150
100
50
0
0.50 0.52 0.54 0.56 0.58
0.50 0.52 0.54 0.56 0.58
0.54 0.55 0.56 0.57 0.58 0.59
0.54 0.55 0.56 0.57 0.58 0.59
Mean anisotropy
Mean Spearman response

Figure 4

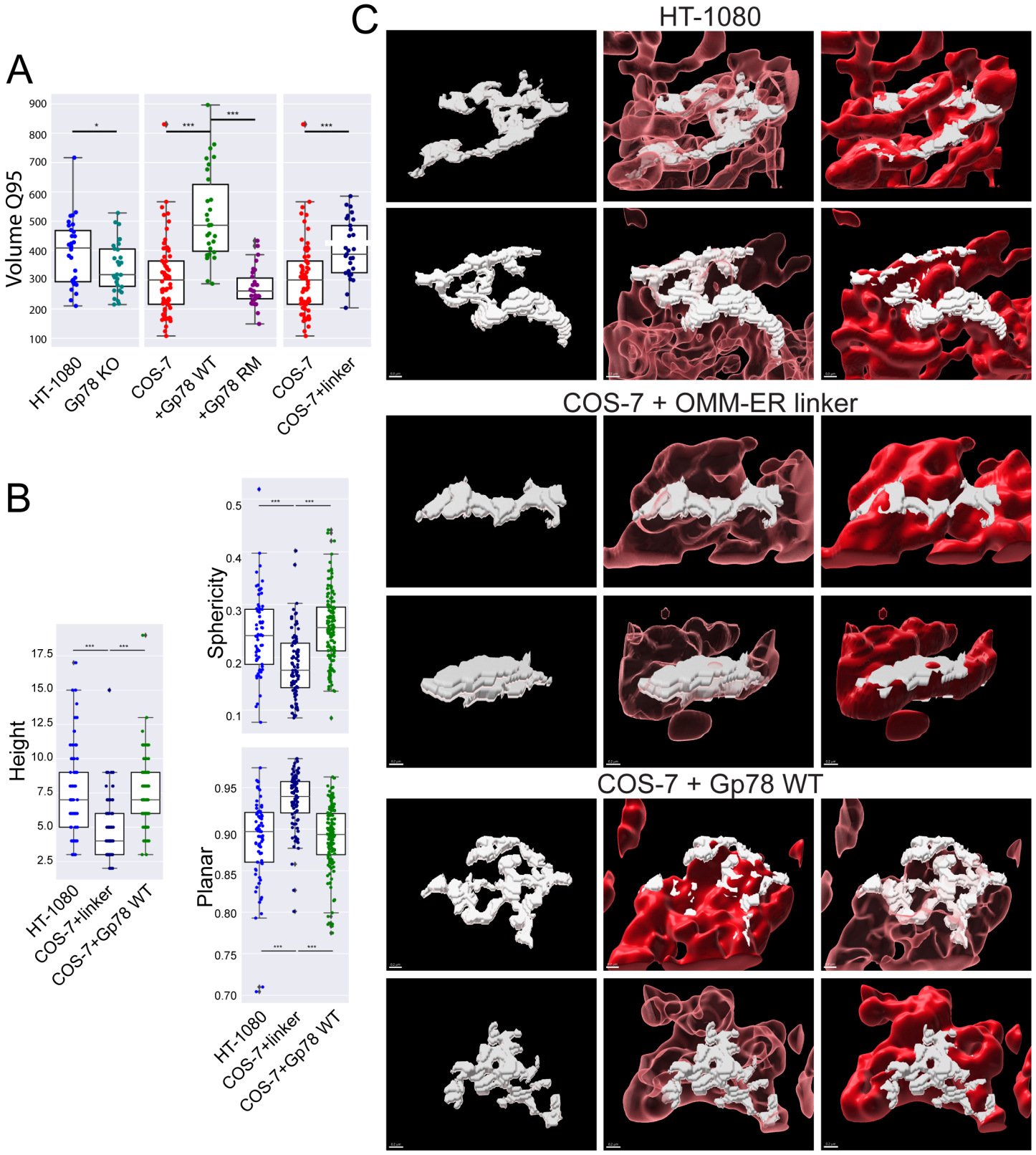
A
Volume Q95
900
800
700
600
500
400
300
200
100
*
***
***
***
HT-1080
Gp78 KO
COS-7
+Gp78 WT
+Gp78 RM
COS-7
COS-7+linker
B
Height
17.5
15.0
12.5
10.0
7.5
5.0
2.5
***
***
HT-1080
COS-7+linker
COS-7+Gp78 WT
Sphericity
0.5
0.4
0.3
0.2
0.1
Planar
0.95
0.90
0.85
0.80
0.75
0.70
C
HT-1080
COS-7 + OMM-ER linker
COS-7 + Gp78 WT

Figure 5